LETTER

doi:10.1038/nature25984

A lithium–oxygen battery with a long cycle life in an air-like atmosphere

Mohammad Asadi[1,2], Baharak Sayahpour[1], Pedram Abbasi[1], Anh T. Ngo[3], Klas Karis[4], Jacob R. Jokisaari[4], Cong Liu[5], Badri Narayanan[3], Marc Gerard[1], Poya Yasaei[1], Xuan Hu[4], Arijita Mukherjee[4], Kah Chun Lau[6], Rajeev S. Assary[3], Fatemeh Khalili-Araghi[4], Robert F. Klie[4], Larry A. Curtiss[3] & Amin Salehi-Khojin[1]

Lithium–air batteries are considered to be a potential alternative to lithium-ion batteries for transportation applications, owing to their high theoretical specific energy[1]. So far, however, such systems have been largely restricted to pure oxygen environments (lithium–oxygen batteries) and have a limited cycle life owing to side reactions involving the cathode, anode and electrolyte[2–5]. In the presence of nitrogen, carbon dioxide and water vapour, these side reactions can become even more complex[6–11]. Moreover, because of the need to store oxygen, the volumetric energy densities of lithium–oxygen systems may be too small for practical applications[12]. Here we report a system comprising a lithium carbonate-based protected anode, a molybdenum disulfide cathode[2] and an ionic liquid/dimethyl sulfoxide electrolyte that operates as a lithium–air battery in a simulated air atmosphere with a long cycle life of up to 700 cycles. We perform computational studies to provide insight into the operation of the system in this environment. This demonstration of a lithium–oxygen battery with a long cycle life in an air-like atmosphere is an important step towards the development of this field beyond lithium-ion technology, with a possibility to obtain much higher specific energy densities than for conventional lithium-ion batteries.

We used two strategies to limit side reactions in a lithium–oxygen battery in a simulated air atmosphere with representative amounts of O_2, N_2, CO_2 and H_2O. First, we developed a Li_2CO_3/C coating for the lithium anode that allows only lithium cations to pass through, thus protecting the anode from the components of the simulated air. Li_2CO_3 was not expected to react with water to produce the bicarbonate, because the reaction is not thermodynamically favourable under ambient conditions (Supplementary Information section 1). Second, we constructed a cathode based on previously reported molybdenum disulfide nanoflakes[2], and a mixture of the ionic liquid 1-ethyl-3-methylimidazolium tetrafluoroborate (EMIM-BF_4) and dimethyl sulfoxide (DMSO) was used as the electrolyte. The components of this system operate in conjunction to prevent the formation of side products in the presence of CO_2 and H_2O.

The Li_2CO_3/C anode-protection coating was directly synthesized on a Li anode in a custom-made electrochemical lithium–carbon dioxide cell filled with pure CO_2; ten continuous discharge–charge cycles were operated to form the protective coating (Supplementary Information section 1). Scanning electron microscopy (SEM) images of the coated anode (Fig. 1a and Supplementary Fig. 2a–c) reveal a dense network of rod-shape structures on the surface. Raman spectra show distinct peaks at 717, 743, 1088 and 1,456 cm^{-1} for this coating (Fig. 1b), which are characteristic peaks of Li_2CO_3 (ref. 13) (Supplementary Information section 3). Moreover, X-ray photoelectron spectroscopy (XPS; Fig. 1c, d and Supplementary Fig. 4a–c) for Li 1*s*, C 1*s* and O 1*s* reveals peaks at 55.2, 289.3 and 531.5 eV, respectively, further confirming the presence of Li_2CO_3 (ref. 14). A peak at 284.8 eV corresponds to bonds between carbon atoms, and is attributed to adventitious carbon compounds as well as solid carbon from the reaction of Li and CO_2 (Supplementary Information section 1). The synthesized Li_2CO_3/C coating was further characterized by electron energy loss spectroscopy (EELS). The K-edge peaks of lithium, oxygen and carbon, obtained from EELS of platelet-like particles extracted from the anode, are presented in Fig. 1e. The sharp peaks corresponding to these elements are similar to those observed for Li_2CO_3 in the solid–electrolyte interphases of lithium-ion batteries[15] (Supplementary Information section 5).

The lithium retention of the protected anode was investigated by running a cell in an air environment for 51 cycles, followed by an exhaustive stripping test, with the results shown in Fig. 1f. This indicated that the protected anode has an average lithium retention of 99.97% per cycle (Supplementary Information section 6). Moreover, electrochemical impedance spectroscopy was used to study the charge-transfer resistance (R_{ct}) of the protective layer (Supplementary Information section 7). The results shown in Fig. 1g indicate that the R_{ct} of the protected anode (formed from ten deposition cycles) is around 550 kΩ, which is about 20 times greater than that of an unprotected anode (30 kΩ), confirming the existence of an electrically insulating protective coating on the surface of the anode.

A custom-made cell with a MoS_2 cathode, a protected lithium anode and an EMIM-BF_4/DMSO (25%/75%) electrolyte was used in the lithium–air experiments (Supplementary Information sections 8–10). This electrolyte composition provides the maximum oxygen reduction and evolution in a three-electrode electrochemical cell (Supplementary Information section 10). A custom-made simulated air stream of around 79% N_2, around 21% O_2, 500 p.p.m. CO_2, and a relative humidity of 45% at 25 °C was used for the battery experiments (Supplementary Information section 11). Figure 2a shows the long-term discharging and charging profiles up to a capacity of 500 mAh g^{-1} with a constant current density of 500 mA g^{-1}. The charge at the first cycle began at 2.92 V, which is very close to the reversible thermodynamic potential of Li_2O_2 formation (2.96 V versus Li/Li^+)[16] and reached a potential of 3.75 V at a capacity of 500 mA g^{-1}. The potential gap for the first cycle of the lithium–air system is 0.88 V, increasing to 1.3 V after 50 cycles, followed by a gradual increase to 1.62 V after 550 cycles. The increase in the potential gap during cycling may be due to slow degradation of the protective anode coating and/or the MoS_2 cathode. We did not observe any failure of the battery during testing for up to 700 cycles (Supplementary Information section 12). Figure 2b shows the dependence of the number of discharge–charge cycles achieved in air on the number of deposition cycles used to form the anode-protection layer. The results indicate a substantial increase in the number of lithium–air cycles achieved when the anode is protected compared with when it is not; with no coating, the lithium–air cell

[1]Department of Mechanical and Industrial Engineering, University of Illinois at Chicago, Chicago, Illinois 60607, USA. [2]Department of Chemical and Biological Engineering, Illinois Institute of Technology, Chicago, Illinois 60616, USA. [3]Materials Science Division, Argonne National Laboratory, Argonne, Illinois 60439, USA. [4]Department of Physics, University of Illinois at Chicago, Chicago, Illinois 60607, USA. [5]Chemical Sciences Division, Argonne National Laboratory, Argonne, Illinois 60439, USA. [6]Department of Physics and Astronomy, California State University, Northridge, California 91330, USA.

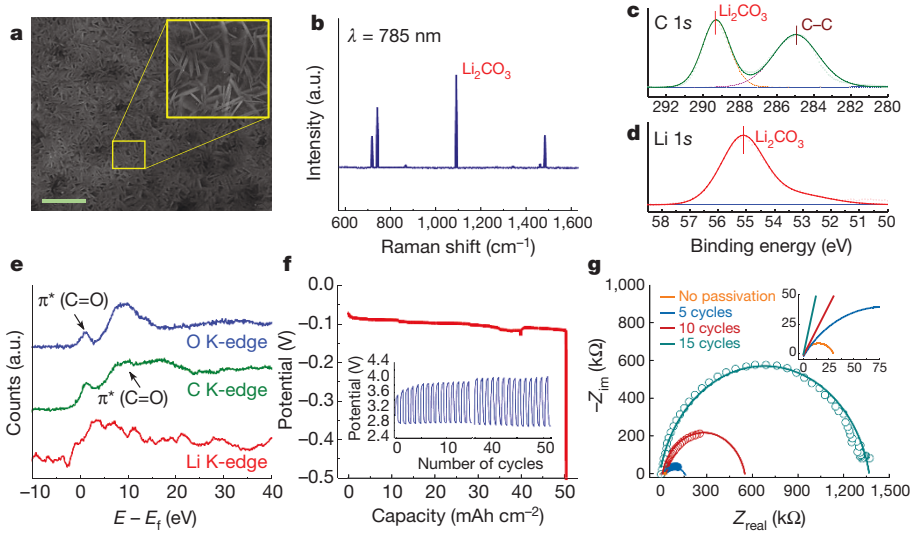

Figure 1 | Characterization of the protected anode. a, SEM image of the protected anode surface (scale bar, 1 μm). **b**, Raman spectrum of the protected anode, excited by a 785-nm laser. **c**, **d**, XPS spectra of the protected anode surface in the Li 1*s* (**c**) and C 1*s* (**d**) regions. **e**, EELS spectra showing the lithium, carbon and oxygen K-edges of the anode surface, consistent with the presence of Li_2CO_3. **f**, Exhaustive stripping of protected lithium using a current density of 0.5 mA cm^{-2}. The inset shows a cycling test of the protected anode in air under a current density of 0.05 mA cm^{-2}. **g**, Electrochemical impedance spectroscopy of the passivated anode after 5, 10 and 15 cycles of exposure to a CO_2 environment, compared to an anode without passivation.

fails after 11 cycles, whereas up to 700 cycles can be achieved with an anode-protection layer. The thickness of the anode-protection layer helps to understand these results. Although the electronic conductivity of thinner coatings can result in electrolyte decomposition, the low ionic conductivity of thicker coatings can result in larger charge potentials and lead to deleterious side reactions. In this case, ten deposition cycles resulted in the optimum thickness to balance these effects.

Raman spectroscopy and XPS were performed on the surface of the cathode to study the discharge products and the cell chemistry after cycling. In terms of lithium species, the Raman spectra (Fig. 2c) show the presence of only a Li_2O_2 peak at 788 cm^{-1}; we did not detect any peaks related to LiOH, Li_2CO_3 or LiO_2, and the Li_2O_2 peaks were not present in the charged samples (Supplementary Information section 13).

To study the possibility of any chemical reactions of the electrolyte with Li_2O_2, we aged a 50-cycle discharged cathode sample in electrolyte for 200 hours; the Raman spectra after ageing did not show any evidence of side products. To further confirm the presence of Li_2O_2, we performed XPS analysis on the cathode surface. Figure 2d–f shows the Li 1*s*, C 1*s* and O 1*s* spectra of the discharged cathode after 250 cycles. The Li 1*s* and O 1*s* peaks of Li_2O_2, at 55.07 and 531.12 eV, respectively, are in agreement with previously reported *in situ* ambient-pressure XPS studies on Li_2O_2 formed in a lithium–oxygen cell[17,18]. The C 1*s* spectra show the reference C–C bond of carbon at 284.8 eV and other carbon peaks at 286.6 and 288.5 eV, which probably arise from the gas diffusion layer. Figure 2d–f also confirms the absence of Li_2CO_3 and LiOH during discharge. Similar XPS results were obtained after one cycle and

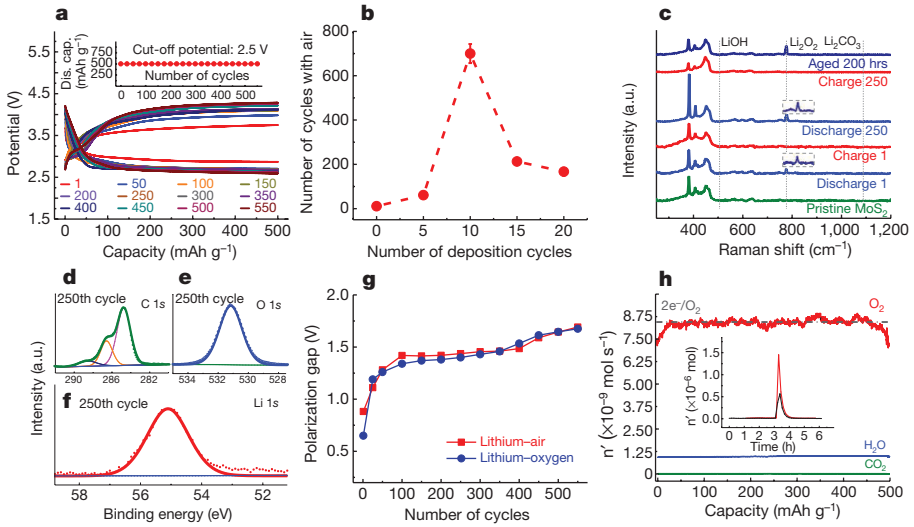

Figure 2 | Performance of the cathode in a lithium–air battery system. a, The discharge–charge voltage profile over 550 cycles. The inset shows the capacity versus the number of cycles. **b**, The dependence of the number of battery cycles achieved in air on the number of deposition cycles used to form the anode-protection layer. The error bar shows the standard deviation of three measurements. **c**, Raman spectra of the cathode after the first and after the 250th discharge–charge cycle, compared to pristine MoS_2 and a 200-hour-aged sample. **d**–**f**, XPS spectra of the cathode surface for C 1*s* (**d**), O 1*s* (**e**) and Li 1*s* (**f**) after the 250th discharge cycle. **g**, The polarization gap between the lithium–air battery and the Li–O_2 battery, measured under the same operating conditions, as a function of cycle number. **h**, DEMS profiles of the cell during the first charging process, after the cell was discharged to 500 mAh g^{-1}. The inset shows the number of moles of oxygen detected by DEMS, before (red line) and after (black line) discharge in the first cycle.

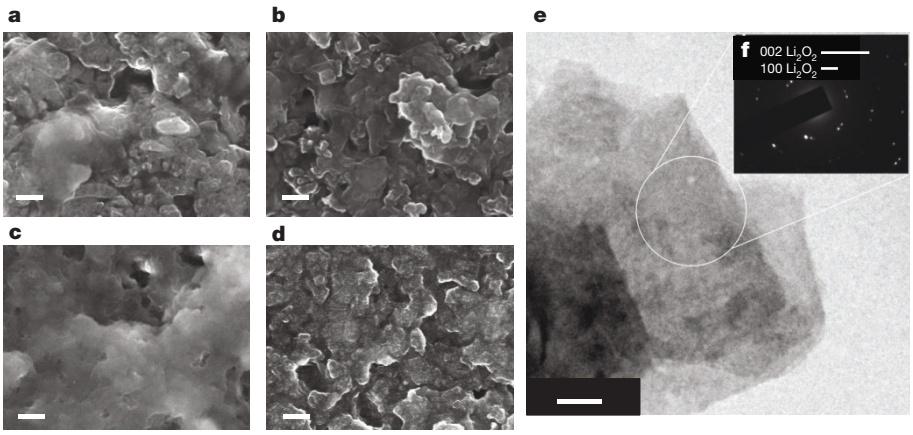

Figure 3 | Electron microscopy of the cathode. a–d, The SEM images of lithium–air battery cathodes after the first discharge (**a**), the first charge (**b**), the 250th discharge (**c**) and the 250th charge (**d**). Scale bars, 200 nm. **e**, TEM image of a discharged cathode sample. **f**, Diffraction pattern showing crystallinity corresponding to monoclinic lithium peroxide, Li_2O_2.

after 100 cycles, and for an aged sample (25 cycles, aged for 100 hours; Supplementary Information section 14).

Additional evidence that the presence of CO_2 and H_2O in our lithium–air cell does not cause any detrimental reactions was obtained from the results of a discharge–charge experiment in a pure oxygen environment, using the same cell as for the aforementioned experiments (Supplementary Information section 15). Figure 2g demonstrates similar results for both the lithium–air and lithium–oxygen batteries, indicating that the discharge and charge chemistries are the same in both systems. To examine the stability of the EMIM-BF_4/DMSO electrolyte in the lithium–air system, we also performed ^{1}H and ^{13}C nuclear magnetic resonance (NMR) spectroscopic studies on both fresh electrolytes and electrolytes after 550 cycles of operation. The ^{1}H NMR and ^{13}C NMR spectra (Supplementary Information section 16) show similar peaks for both samples, verifying the stability of the electrolyte during operation of the cell.

The electrochemical reaction during the charge and discharge processes was quantified by *in situ* monitoring of the evolved and consumed gases, respectively, during the first cycle using differential electrochemical mass spectrometry (DEMS)[2,4,19,20] (Supplementary Information section 17). The DEMS results shown in Fig. 2h indicate an electron/oxygen ratio of 2.07 for the charge reaction and 2.04 for the discharge reaction. These results provide strong evidence for the reversible formation and decomposition of Li_2O_2 as the main product, through a two-electron transfer process.

The morphology and composition of the discharge product was studied using several techniques. SEM images of the cathodes after the 1st and 250th cycles (Fig. 3a–d) indicate a film-like morphology of the discharge products on the cathode surface. This was also observed for samples after 100 cycles (Supplementary Information section 18). X-ray diffraction experiments performed on the discharge product after 550 cycles revealed distinct peaks at 32° and 34°, which were attributed to crystalline (100) and (101) facets of Li_2O_2 (Supplementary Information section 19)[2,3]. Finally, TEM images and diffraction patterns obtained from the cathode (Fig. 3e, f) show the discharge product to be highly crystalline, with the diffraction pattern corresponding to Li_2O_2 viewed along a *c*-axis direction. Scanning transmission electron microscopy (STEM) imaging was also used to confirm the morphology of the discharge product, showing that Li_2O_2 has a thin film-like structure that consists of extended single crystal domains. EELS spectroscopy was performed on a sample of the discharge product taken from the Li_2O_2 film, and revealed a Li K-edge fine structure consistent with reference Li_2O_2 samples that are stoichiometric and largely free of oxygen vacancies (Supplementary Information section 20).

We carried out density functional theory (DFT) calculations to provide insight into why the cell configuration used in this study can operate in the presence of air. We investigated the Li_2CO_3 anode coating and its ability to prevent reactions of lithium metal with N_2 and O_2; the possible reactions of CO_2 and H_2O with the discharge product at the cathode; and the possible side reactions in the electrolyte with discharge species. DFT calculations concerning the catalytic role of the molybdenum-terminated edge atoms of MoS_2 nanoflakes in the presence of the ionic-liquid electrolyte in a lithium–oxygen battery have been previously reported[2].

To investigate the role of the anode, DFT calculations (Supplementary Information section 21.1) were carried out on a Li_2CO_3/Li interface (Supplementary Information section 21.2). The relaxed Li_2CO_3/Li interface with carbon termination—the most stable termination—is shown in Fig. 4a. Although lithium and Li_2CO_3 are thermodynamically unstable with respect to Li_2O and carbon[21], the interface appears to be kinetically stable based on the barrier for oxygen migration from a C–O bond to lithium; a barrier of 1.1 eV is found for this reaction pathway (Fig. 4b). In addition, we investigated whether N_2 and O_2 were likely to migrate through Li_2CO_3 by placing them in the (010) channel of Li_2CO_3 (Fig. 4c) and calculating the energy for the relaxed structure relative to the Li_2CO_3 and the free molecules (Supplementary Information section 21.3). The energies were found to be high (1.2–3.2 eV), which indicates that Li_2CO_3 should provide a good barrier to prevent N_2 and O_2 from reaching the lithium anode, assuming no cracks in the structure. Li_2CO_3 should therefore also prevent oxygen crossover—in which oxygen crosses from the cathode to the anode—which is known to result in oxidation of the lithium anode and to limit cycle life[5]. Because H_2O and CO_2 molecules are larger than N_2 and O_2, their interactions with Li_2CO_3 channels should also be endothermic. On the basis of previous DFT calculations for lithium-ion batteries[22,23], the diffusion of lithium through Li_2CO_3 should be quite facile, unlike that of N_2 and O_2.

The second aspect of our computational studies used DFT calculations to investigate possible detrimental reactions of CO_2 and H_2O with the Li_2O_2 discharge product. We have assumed that the nitrogen will not react with the discharge product, owing to its inertness. The SEM and TEM studies indicated that the Li_2O_2 product has a film-like morphology with few defects. The film-like Li_2O_2 discharge product is consistent with its postulated formation mechanism proposed in a previous study of a MoS_2 cathode material for a lithium–oxygen cell.[2] DFT calculations (Supplementary Information sections 21.4 and 21.5) indicate considerable binding of a Li_2O_2 molecule and Li_2O_2 cluster to the basal plane of a MoS_2 nanoflake, which could provide sites for the nucleation and growth of Li_2O_2. The interaction of a Li_2O_2 molecule with the MoS_2 basal plane is shown in Fig. 4d. The high dielectric constant of the ionic liquid/DMSO electrolyte means that LiO_2 is sufficiently soluble[24] to enable a solution growth mechanism[25]. Finally, the high discharge rate could contribute to the formation of the thin film found in our cell[26,27]. This is important because a Li_2O_2 film is expected to have fewer defect sites compared to other morphologies such as

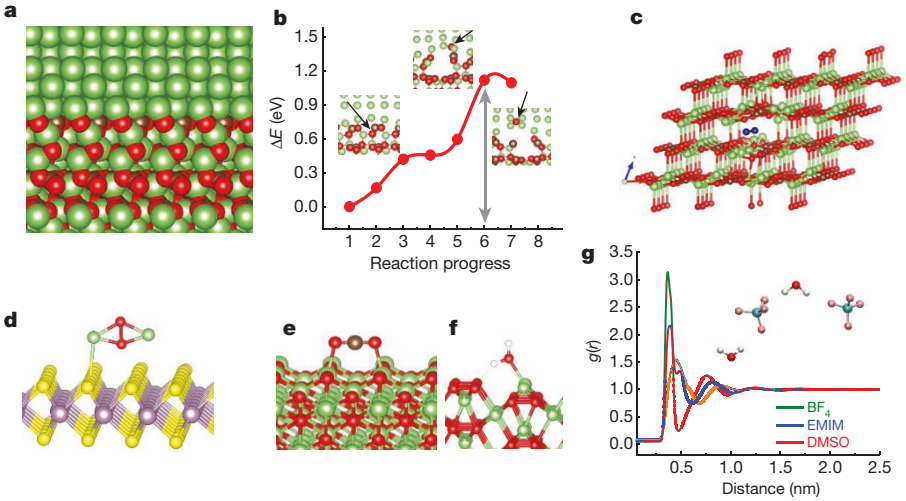

Figure 4 | Computational study of the anode, cathode and electrolyte of the lithium–air battery cell. a, Interface between (001) Li_2CO_3 and (100) Li with carbon termination, as calculated by DFT. **b**, DFT profile showing the breaking of the C–O bond of Li_2CO_3 at the interface, and the migration of oxygen to the lithium bulk (black arrows indicate oxygen). **c**–**f**, Depiction of interactions relevant to the lithium–air battery cell, as calculated by DFT: O_2 in the Li_2CO_3 channel, endothermic by 3.1 eV (**c**); Li_2O_2 on the MoS_2-nanoflake basal plane, binding energy 0.83 eV (**d**); CO_2 on the (100) Li_2O_2 surface, binding energy 0.27 eV (**e**); H_2O on the (100) Li_2O_2 surface, binding energy 0.77 eV (**f**). **g**, Classical molecular dynamics radial distribution function showing the interaction of water with BF_4^-, $EMIM^+$ and DMSO, calculated from the trajectory of a system at 2 mol% water.

nanoparticles or toroids[28], thereby reducing decomposition reactions involving CO_2 and H_2O.

To investigate possible reactions of H_2O and CO_2 with the Li_2O_2 surface expected for a thin-film morphology, we carried out DFT calculations of H_2O and CO_2 adsorbed on various relaxed Li_2O_2 surfaces[29] in the presence and absence of an electrolyte (Supplementary Information sections 21.6 and 21.7). The most stable structures in the absence of electrolyte are shown in Fig. 4e, f. The strongest adsorption energies for CO_2 and H_2O on the Li_2O_2 surfaces are 0.27 and 0.77 eV, respectively. According to the calculations, neither H_2O nor CO_2 decompose when adsorbed on the Li_2O_2 surfaces. We also included the electrolyte in the calculations in *ab initio* molecular dynamics simulations. The simulations with the electrolyte/Li_2O_2 interface did not show any specific preference for CO_2 or H_2O to adsorb on the surface or remain in the electrolyte. These results are consistent with calculations of the solvation energies of H_2O and CO_2 in the ionic liquid/DMSO electrolyte, indicating reasonably strong binding in the ionic liquid (Supplementary Information section 21.8). The solvation energies in solution are at least as strong or stronger than the binding to the Li_2O_2 surface. Furthermore, in the presence of the electrolyte, the adsorbed species at the interface do not react with the Li_2O_2 surface.

We also carried out *ab initio* molecular dynamics simulations for CO_2 and H_2O molecules interacting with a defective Li_2O_2 surface containing a single lithium vacancy, in the presence of a mixed ionic liquid/DMSO electrolyte, and found no decomposition such as that which may occur on toroid discharge products (Supplementary Information section 21.7). All of the computational results of the reaction of H_2O and CO_2 with a Li_2O_2 surface are consistent with the lack of evidence for side reactions in the characterization studies.

Finally, we considered side reactions involving the probable discharge species, LiO_2 and Li_2O_2, with CO_2 or H_2O in the electrolyte using classical molecular dynamics simulations (Supplementary Information section 22.1). The peaks in the radial distribution function in Fig. 4g show the interaction of water molecules with BF_4 and DMSO from the solvent. Further analysis of hydrogen bonds between these species show that approximately 72% of the water molecules are involved in small clusters of BF_4, DMSO and H_2O, all connected through hydrogen bonds (Supplementary Information section 22.2). A representative cluster is shown in the inset of Fig. 4g. Our DFT calculations (Supplementary Information section 22.2) show that the reactions of water with Li_2O_2 or LiO_2 are thermodynamically unfavourable, and reaction with two water molecules would be required. However, the classical molecular dynamics simulations show that, at 2 mol% of water, clusters of two or more water molecules occur only less than 3% of the time. Therefore, there is very little likelihood of the LiO_2 or Li_2O_2 solvated species encountering a water cluster. In the case of CO_2, the reaction with Li_2O_2 or LiO_2 is thermodynamically favourable but requires reaction with two or more CO_2 molecules; such clusters are highly unlikely (less than 0.2%) based on the classical molecular dynamics simulations.

In summary, the characterization and computational studies have shown that the protected lithium anode, electrolyte blend and high-performance air cathode all work in synergy to provide a lithium–oxygen battery with a long cycle life under simulated air conditions. This new architecture is a promising step towards engineering the next generation of lithium batteries with much higher specific energy density than current lithium-ion batteries.

Online Content Methods, along with any additional Extended Data display items and Source Data, are available in the online version of the paper; references unique to these sections appear only in the online paper.

Received 12 February 2017; accepted 30 January 2018.

1. Bruce, P. G., Freunberger, S. A., Hardwick, L. J. & Tarascon, J.-M. Li–O_2 and Li–S batteries with high energy storage. *Nat. Mater.* **11,** 19–29 (2012).
2. Asadi, M. *et al.* Cathode based on molybdenum disulfide nanoflakes for lithium–oxygen batteries. *ACS Nano* **10,** 2167–2175 (2016).
3. Jung, H.-G., Hassoun, J., Park, J.-B., Sun, Y.-K. & Scrosati, B. An improved high-performance lithium–air battery. *Nat. Chem.* **4,** 579–585 (2012).
4. Lu, J. *et al.* A nanostructured cathode architecture for low charge overpotential in lithium–oxygen batteries. *Nat. Commun.* **4,** 2383 (2013).
5. Assary, R. S. *et al.* The effect of oxygen crossover on the anode of a Li–O_2 battery using an ether-based solvent: insights from experimental and computational studies. *ChemSusChem* **6,** 51–55 (2013).
6. Geng, D. *et al.* From lithium–oxygen to lithium–air batteries: challenges and opportunities. *Adv. Energy Mater.* **6,** 1502164 (2016).
7. Christensen, J. *et al.* A critical review of Li/air batteries. *J. Electrochem. Soc.* **159,** R1–R30 (2012).
8. Garcia-Araez, N. & Novák, P. Critical aspects in the development of lithium–air batteries. *J. Solid State Electrochem.* **17,** 1793–1807 (2013).
9. Zhang, T. & Zhou, H. A reversible long-life lithium–air battery in ambient air. *Nat. Commun.* **4,** 1817 (2013).
10. Das, S. K., Chai, J., Rahman, S. & Sarkar, A. Synthesis, characterization and performance evaluation of an advanced solid electrolyte and air cathode for rechargeable lithium–air batteries. *J. Mater. Sci. Chem. Eng.* **4,** 74–89 (2016).

11. Wu, S. *et al.* A synergistic system for lithium–oxygen batteries in humid atmosphere integrating a composite cathode and a hydrophobic ionic liquid-based electrolyte. *Adv. Funct. Mater.* **26,** 3291–3298 (2016).
12. Gallagher, K. G. *et al.* Quantifying the promise of lithium–air batteries for electric vehicles. *Energy Environ. Sci.* **7,** 1555–1563 (2014).
13. Pasierb, P., Komornicki, S., Rokita, M. & Rękas, M. Structural properties of Li_2CO_3–$BaCO_3$ system derived from IR and Raman spectroscopy. *J. Mol. Struct.* **596,** 151–156 (2001).
14. Bi, Y. *et al.* Stability of Li_2CO_3 in cathode of lithium ion battery and its influence on electrochemical performance. *RSC Advances* **6,** 19233–19237 (2016).
15. Sina, M. *et al.* Investigation of SEI layer formation in conversion iron fluoride cathodes by combined STEM/EELS and XPS. *J. Phys. Chem. C* **119,** 9762–9773 (2015).
16. Imanishi, N., Luntz, A. C. & Bruce, P. (eds) *The Lithium Air Battery: Fundamentals* (Springer, 2014).
17. Du, P. *et al.* Compatibility of lithium salts with solvent of the non-aqueous electrolyte in Li–O_2 batteries. *Phys. Chem. Chem. Phys.* **15,** 5572–5581 (2013).
18. Lu, Y.-C. *et al.* In situ ambient pressure X-ray photoelectron spectroscopy studies of lithium–oxygen redox reactions. *Sci. Rep.* **2,** 715 (2012).
19. McCloskey, B. D., Bethune, D. S., Shelby, R. M., Girishkumar, G. & Luntz, A. C. Solvents' critical role in nonaqueous lithium–oxygen battery. *J. Phys. Chem. Lett.* **2,** 1161–1166 (2011).
20. Lu, J. *et al.* A lithium–oxygen battery based on lithium superoxide. *Nature* **529,** 377–382 (2016).
21. Leung, K., Soto, F., Hankins, K., Balbuena, P. B. & Harrison, K. L. Stability of solid electrolyte interphase components on lithium metal and reactive anode material surfaces. *J. Phys. Chem. C* **120,** 6302–6313 (2016).
22. Iddir, H. & Curtiss, L. A. Li ion diffusion mechanisms in bulk monoclinic Li2CO3 crystals from density functional. *J. Phys. Chem. C* **114,** 20903–20906 (2010).
23. Shi, S., Qi, Y., Li, H. & Hector, L. G. Defect thermodynamics and diffusion mechanisms in Li_2CO_3 and implications for the solid electrolyte interphase in Li-ion batteries. *J. Phys. Chem. C* **117,** 8579–8593 (2013).
24. Cheng, L. *et al.* Computational studies of solubilities of LiO_2 and Li_2O_2 in aprotic solvents. *J. Electrochem. Soc.* **164,** E3696–E3701 (2017).
25. Johnson, L. *et al.* The role of LiO_2 solubility in O_2 reduction in aprotic solvents and its consequences for Li–O_2 batteries. *Nat. Chem.* **6,** 1091–1099 (2014).
26. Welland, M. J. *et al.* An atomistically informed mesoscale model for growth and coarsening during discharge in lithium–oxygen batteries. *J. Chem. Phys.* **143,** 224113 (2015).
27. Adams, B. D. *et al.* Current density dependence of peroxide formation in the Li–O_2 battery and its effect on charge. *Energy Environ. Sci.* **6,** 1772 (2013).
28. Xiao, D. *et al.* Direct observation of ordered oxygen defects on the atomic scale in Li_2O_2 for Li–O_2 batteries. *Adv. Energy Mater.* **5,** 1400664 (2015).
29. Lau, K. C., Curtiss, L. A. & Greeley, J. Density functional investigation of the thermodynamic stability of lithium oxide bulk crystalline structures as a function of oxygen pressure. *J. Phys. Chem. C* **115,** 23625–23633 (2011).

Supplementary Information is available in the online version of the paper.

Acknowledgements The work of A.S.-K., M. A., B. S. and P. A. was supported by the National Science Foundation (NSF-DMREF Award #1729420). Work by B.N., K.C.L., R.S.A., L.A.C., R.F.K., A.M., X. H. and J.R.J. was supported by the Joint Center for Energy Storage Research (JCESR), an Energy Innovation Hub funded by the US Department of Energy, Office of Science, Basic Energy Sciences. Work by A.N. and C.L. was supported by the Center for Electrical Energy Storage: Tailored Interfaces, an Energy Frontier Research Center funded by the US Department of Energy, Office of Science, Office of Basic Energy Sciences. The work of F.K.A. and K.K. was supported by a University of Illinois at Chicago start-up fund. C.L. was also supported by programme development funds provided by the Chemical Sciences and Engineering division at Argonne National Laboratory. We acknowledge the MRSEC Materials Preparation and Measurement Laboratory shared user facility at the University of Chicago (NSFDMR-1420709); the EPIC facility (NUANCE Center, Northwestern University), which has received support from the MRSEC program (NSF DMR-1121262) at the Materials Research Center; the Nanoscale Science and Engineering Center (NSF EEC–0647560) at the International Institute for Nanotechnology; and the State of Illinois, through the International Institute for Nanotechnology. This work also made use of the Integrated Molecular Structure Education and Research Center at Northwestern University, which has received support from the Soft and Hybrid Nanotechnology Experimental (SHyNE) Resource (NSF NNCI-1542205). The acquisition of the UIC JEOL JEM ARM200CF was supported by an MRI-R^2 grant from the National Science Foundation (DMR-0959470). The use of instrumentation at University of Illinois at Chicago Research Resources Center (RRC-East) is acknowledged. A. Nicholls at UIC's Electron Microscopy Service is also acknowledged for help and support. This research used high performance computing resources of the Argonne Leadership Computing Facility, which is a DOE Office of Science User Facility supported under Contract DE-AC02-06CH11357. Use of the Center for Nanoscale Materials, an Office of Science user facility, was supported by the US Department of Energy, Office of Science, Office of Basic Energy Sciences, under contract DE-AC02-06CH11357. F.K.A. acknowledges the use of the University of Illinois at Chicago High Performance Computing Cluster to perform molecular dynamics simulations. We thank K. Gallagher, P. Redfern, H.-H. Wang, J. Jureller and X. Chen.

Author Contributions A.S.-K. and M.A. conceived the idea. M.A., B.S., P.A. and M.G. performed the electrochemical experiments. M.A. and B.S. synthesized the MoS_2 nanoflakes. M.A., B.S., P.A. and P.Y. carried out characterization. A.S.-K. supervised the electrochemical experiments. B.N., K.C.L., R.S.A. and L.A.C. carried out the computational studies of electrolytes. C.L. and A.T.N. performed computational studies of surfaces and the Li_2CO_3 coating. J.R.J., X.H., A.M. and R.F.K. carried out STEM and EELS experiments. K.K. and F.K.-A. performed classical molecular dynamics simulations. All of the authors contributed to the manuscript before submission.

Author Information Reprints and permissions information is available at www.nature.com/reprints. The authors declare competing financial interests: details are available in the online version of the paper. Readers are welcome to comment on the online version of the paper. Publisher's note: Springer Nature remains neutral with regard to jurisdictional claims in published maps and institutional affiliations. Correspondence and requests for materials should be addressed to L.A.C. (curtiss@anl.gov) or A.S.-K. (salehikh@uic.edu).

Reviewer Information *Nature* thanks S. Soon, G. Yu and the other anonymous reviewer(s) for their contribution to the peer review of this work.

METHODS

Anode preparation. The battery cell was assembled using commercial pure lithium chips (>99.9%) with a thickness of 0.25 mm as the anode, and MoS_2 nanoflakes coated on a gas diffusion layer as the cathode. The electrolyte of the cell was composed of 25 vol% 1-ethyl-3-methylimidazolium tetrafluoroborate (EMIM-BF_4) (HPLC grade, >99.0%) and 75 vol% dimethyl sulfoxide (DMSO) with 0.1 M lithium bis(trifluoromethanesulfonyl)imide (LiTFSI) (>99.0%) as a lithium salt. The cell was run for ten continuous cycles, each cycle consisting of a one-hour charge process followed by a one-hour discharge process, in an environment of pure CO_2.

Cathode preparation. The MoS_2 nanoflakes were synthesized using a liquid exfoliation method[2], in which 300 mg of MoS_2 powder (99%) was dispersed in 60 ml isopropyl alcohol (>99.5%). The solution was exfoliated for 20 h and centrifuged for 1 h to extract the supernatant (the top two-thirds of the centrifuged solution). MoS_2 nanoflakes were then coated on a conductive substrate of the gas diffusion layer (0.2 mm thickness, 80% porosity) to reach a catalyst loading of 0.1 mg cm^{-2}. Prepared cathodes were dried in a vacuum oven for 24 h at 80 °C to stabilize the cathode and to remove impurities.

Electrochemical characterization. Electrochemical impedance spectroscopy experiments were performed using coin cells under identical experimental conditions of 700 mV overpotential and a frequency range of 10 Hz to 100 kHz.

For discharge–charge experiments, the lithium–air Swagelok battery set-up consisting of MoS_2 nanoflakes as the cathode, 0.1 M LiTFSI as the lithium salt in EMIM-BF_4:DMSO (25:75 volume ratio) as the electrolyte, and protected lithium as the anode was operated with a constant applied current density of 500 mA g^{-1}.

Characterization techniques. Raman spectroscopy experiments were performed using a Horiba LabRAM HR Evolution confocal Raman microscope. The samples were sealed between two transparent glasses in an argon-filled glove box. The instrument was configured with a 785-nm laser source, 1,200 g mm^{-1} grating, a Horiba Andor detector and a LCD objective with a modifiable optical ring that enables aberration correction according to glass thickness.

X-ray photoelectron spectroscopy experiments were performed on a Thermo Scientific ESCALAB 250Xi instrument. The instrument was equipped with an electron flood and scanning ion gun. To prevent oxidation and any contamination, a mobile glove box filled with argon was used for transferring the samples into the loading chamber of the instrument.

The DEMS experiment was carried out in a custom-made Swagelok battery set-up. The experimental set-up consisted of a potentiostat (MTI) and a mass spectrometer (Hiden Analytical) operating under ultra-high vacuum. The DEMS was calibrated by injecting into the mass spectrometer standard samples of pure O_2 (99.99%, Praxair) in research-grade argon (99.99%, Praxair) at known concentrations, and measuring the corresponding partial pressures of O_2.

STEM measurements were carried out on an aberration-corrected JOEL JEM-ARM200CF instrument equipped with a cold field-emission electron source and a post-column Gatan Enfina EELS spectrometer. An acceleration voltage of 80 kV was used for both imaging and EELS to reduce beam-induced damage and contamination.

Theoretical methods. Periodic calculations of the surface interactions and Li_2CO_3/Li interfaces were carried out with the Vienna *ab initio* simulation package (VASP)[30] code with plane wave basis sets and projector-augmented wave pseudopotentials[31]. The exchange-correlation functional was treated within the generalized gradient approximation of Perdew-Burke-Ernzerhof [32]. *Ab initio* molecular dynamics simulations of the electrolyte were performed within the generalized gradient approximation using plane-wave basis sets as implemented in VASP[30]. Similar to the static calculations, we described the exchange correlation via Perdew–Burke–Ernzerhof functionals[32] and use projector-augmented wave pseudopotentials[31] supplied by VASP for the *ab initio* molecular dynamics simulations. For details of specific calculations, see Supplementary Information section 21.

Quantum chemical calculations were carried out to investigate the thermodynamic stability of solvated structures of CO_2 and H_2O using the Gaussian09 code[33], using the 6-31+G(d,p) basis set with the B3LYP functional.

Classical molecular dynamics simulations were carried out using the software package GROMACS 5[34,35] with the GROMOS 53A6 force field[36]. To represent atomic interactions of water molecules, we used the SPC[37] as well as the SPC/E[38] water models owing to their considerably different self-diffusion coefficients[38–40]. All simulations were carried out using isotropic constant pressure control using the Berendsen Barostat[41], with a coupling constant of 1.0 ps and a compressibility of 2.755×10^{-5} bar^{-1} used for all equilibrium and production simulations. Temperature was maintained at 300 K using a Berendsen Thermostat[41], with a coupling constant of 0.1 ps and a time step of 1 fs. The Verlet cut-off scheme was used. Coulomb interactions were calculated using the particle mesh Ewald method with a Coulomb radius set to 1.4 nm. Van der Waals forces were evaluated using a switching function from 0.8 to 1.4 nm.

Data availability. The data that support the findings of this study are available from the corresponding authors upon reasonable request.

30. Kresse, G. & Furthmüller, J. Efficiency of *ab-initio* total energy calculations for metals and semiconductors using a plane-wave basis set. *Comput. Mater. Sci.* **6,** 15–50 (1996).
31. Kresse, G. From ultrasoft pseudopotentials to the projector augmented-wave method. *Phys. Rev. B* **59,** 1758–1775 (1999).
32. Perdew, J. P., Burke, K. & Ernzerhof, M. Generalized gradient approximation made simple. *Phys. Rev. Lett.* **77,** 3865–3868 (1996).
33. Frisch, M. J. *et al.* Gaussian 09, Revision D.01. (Gaussian Inc., 2009).
34. Berendsen, H. J. C., van der Spoel, D. & van Drunen, R. GROMACS: A message-passing parallel molecular dynamics implementation. *Comput. Phys. Commun.* **91,** 43–56 (1995).
35. Abraham, M. J. *et al.* GROMACS: High performance molecular simulations through multi-level parallelism from laptops to supercomputers. *SoftwareX* **1–2,** 19–25 (2015).
36. Horta, B. A. C. *et al.* A GROMOS-compatible force field for small organic molecules in the condensed phase: the 2016H66 parameter set. *J. Chem. Theory Comput.* **12,** 3825–3850 (2016).
37. Berendsen, H. J. C. *et al.* in *Intermolecular Forces* Vol. 14 (ed. Pullman, B.) 331–342 (Springer, 1981).
38. Berendsen, H. J. C., Grigera, J. R. & Straatsma, T. P. The missing term in effective pair potentials. *J. Phys. Chem.* **91,** 6269–6271 (1987).
39. Mark, P. & Nilsson, L. Structure and dynamics of liquid water with different long-range interaction truncation and temperature control methods in molecular dynamics simulations. *J. Comput. Chem.* **23,** 1211–1219 (2002).
40. Mark, P. & Nilsson, L. Structure and dynamics of the TIP3P, SPC, and SPC/E water models at 298 K. *J. Phys. Chem. A* **105,** 9954–9960 (2001).
41. Berendsen, H. J. C., Postma, J. P. M., van Gunsteren, W. F., DiNola, A. & Haak, J. R. Molecular dynamics with coupling to an external bath. *J. Chem. Phys.* **81,** 3684–3690 (1984).